Microporous and Mesoporous Materials 372 (2024) 113096

Contents lists available at ScienceDirect

Microporous and Mesoporous Materials

journal homepage: www.elsevier.com/locate/micromeso

Squaraine-loaded mesoporous silica nanoparticles for antimicrobial Photodynamic Therapy against bacterial infection

Degnet Melese Dereje [a,b,1], Ana García [c,d,1], Carlotta Pontremoli [a], Blanca González [c,d], Montserrat Colilla [c,d], María Vallet-Regí [c,d], Isabel Izquierdo-Barba [c,d,**], Nadia Barbero [a,e,*]

[a] Department of Chemistry, NIS Interdepartmental and INSTM Reference Centre, University of Torino, Via G. Quarello 15A, 10135, Torino, Italy
[b] Department of Chemical Engineering, Bahir Dar Institute of Technology, Bahir Dar University, Polypeda 01, 0026, Bahir Dar, Ethiopia
[c] Department of Chemistry in Pharmaceutical Sciences, Faculty of Pharmacy, Universidad Complutense de Madrid, Research Institute Hospital 12 de Octubre (i+12), Plaza Ramón y Cajal s/n, 28040, Madrid, Spain
[d] Networking Research Centre on Bioengineering, Biomaterials and Nanomedicine (CIBER-BBN), Spain
[e] Istituto di Scienza, Tecnologia e Sostenibilità per lo Sviluppo dei Materiali Ceramici (ISSMC-CNR), Faenza, RA, Italy

ARTICLE INFO

Keywords:
Antimicrobial Photodynamic Therapy (aPDT)
Mesoporous silica nanoparticles (MSNs)
Squaraine dyes (SQs)
Gram-positive bacteria
Gram-negative bacteria

ABSTRACT

Antimicrobial photodynamic therapy (aPDT) shows promise as a complementary or alternative approach to conventional antimicrobial treatments. Despite possessing some key advantages, many challenges remain, such as optimizing the delivery of photosensitizers, improving light penetration into tissues, and determining the most effective combinations of photosensitizers and light wavelengths for different infections. Moreover, addressing the challenges associated with the aggregation tendency and poor solubility of some photosensitizers, squaraine dyes (SQs) in particular, is crucial for unlocking their full potential in biomedical applications.

This contribution focuses on designing innovative nanophotosensitizers with antimicrobial properties using mesoporous silica nanoparticles (MSNs) loaded with a SQ dye (*i.e.* Br-SQ). MSNs before and after Br-SQ loading were deeply characterized using different techniques, proving the successful incorporation of the dye into the nanocarriers. Upon visible light (640 nm) irradiation, these nanosystems demonstrated remarkable antibacterial activities against both Gram-positive *Staphylococcus aureus* (*S. aureus*) and Gram-negative *Escherichia coli* (*E. coli*).

Our results confirmed that MSNs are valuable nanocarriers of hydrophobic photosensitizers, such as Br-SQ, bringing up new opportunities to develop antibiotic-free nanoformulations to treat bacterial infection while minimizing the risk of antimicrobial resistance.

1. Introduction

The escalating global crisis of antibiotic-resistant (AMR) bacterial infections poses a serious threat to public health worldwide, prompting a critical need for innovative therapeutic approaches [1]. Traditional antibiotic therapies are increasingly losing their efficacy due to the rapid development of resistance mechanisms by pathogens, leading to treatment failures, prolonged illnesses, and increased mortality rates [2,3]. Consequently, there is a pressing need to develop alternative strategies that can effectively fight drug-resistant microbial strains. Antimicrobial photodynamic therapy (aPDT) has emerged as a promising and versatile approach for microbial inactivation without the risk of antibiotic resistance [4–7]. aPDT harnesses the potent bactericidal and fungicidal properties of reactive oxygen species (ROS), generated through the interaction of a photosensitizer with light of specific wavelengths. Upon irradiation, the photosensitizer absorbs photons and undergoes electronic transitions, ultimately producing ROS, such as singlet oxygen and superoxide radicals. These ROS are highly cytotoxic and can rapidly damage essential cellular components, including proteins, lipids, and nucleic acids, leading to microbial death. Importantly, aPDT offers

* Corresponding author. Department of Chemistry, NIS Interdepartmental and INSTM Reference Centre, University of Torino, Via G. Quarello 15A, 10135, Torino, Italy.
** Corresponding author. Department of Chemistry in Pharmaceutical Sciences, Faculty of Pharmacy, Universidad Complutense de Madrid, Research Institute Hospital 12 de Octubre (i+12), Plaza Ramón y Cajal s/n, 28040, Madrid, Spain.
E-mail addresses: ibarba@ucm.es (I. Izquierdo-Barba), nadia.barbero@unito.it (N. Barbero).
[1] Both authors contributed equally to the manuscript.

https://doi.org/10.1016/j.micromeso.2024.113096
Received 8 January 2024; Received in revised form 15 March 2024; Accepted 19 March 2024
Available online 20 March 2024

several advantages over conventional antibiotics, including its ability to target a broad range of pathogens, irrespective of their antibiotic resistance profiles, since the generated singlet oxygen and free radicals do not target specific cellular components that can easily mutate to confer resistance. Moreover, aPDT can be used in combination with conventional antibiotics to enhance treatment outcomes and reduce the risk of resistance development [8–11].

However, the successful application of aPDT depends critically on the selection and delivery of an appropriate photosensitizer. Photosensitizers (PSs) are central components in aPDT, serving as the key agents responsible for the generation of ROS upon exposure to specific wavelengths of light. The choice of photosensitizer plays a pivotal role in the success of aPDT, as it influences several crucial factors, including selectivity, efficiency, photostability, and the spectral properties that dictate the optimal light source for activation [12]. Among the different PSs, polymethine dyes such as cyanines and squaraines (SQs) have garnered significant attention due to their unique optical properties for wide application in various fields of science and technology, such as PDT and imaging [13–16], protein detection [17–19], luminescence solar concentrator [20], dye-sensitized solar cells [21,22].

Even if SQs have been proposed as photosensitizers since more than 20 years, just few works related to their effective use as photosensitizers in PDT are present in literature [15,23], even fewer for aPDT [24–27]. These dyes are characterized by high molar absorptivity and can be easily designed to have absorption maxima in the NIR region (650–900 nm), which allows for deeper tissue penetration compared to shorter wavelengths, enabling the treatment of infections located at greater depths within the body. In addition, SQs exhibit excellent photostability, which is crucial for aPDT since prolonged exposure to light is often necessary to achieve the desired therapeutic effect. Moreover, their ability to fast generate ROS at relatively low concentrations is advantageous for reducing potential off-target effects [14,15].

Despite their many advantages, there are challenges associated with the use of SQs as photosensitizers: proper formulation and delivery of the dyes are essential to ensure their solubility and stability in biological media, selective accumulation, and controlled release at the infection site.

In this context, nanotechnology has emerged as a promising avenue for improving the delivery of photosensitizers, enhancing their stability, and optimizing their pharmacokinetics [28–31].

Recently, our research group published a work related to the incorporation of a brominated SQ into quatsomes nanoparticles, demonstrating how this incorporation overcomes the low water solubility limitation of the brominated SQ without compromising its ability to quickly generate ROS [32]. Moreover, the photodynamic effect has been maximized due to the highly localized SQ loading in the QS, allowing to use a therapeutic SQ concentration 100 lower times compared to the concentration of free SQ usually employed in PDT. In another work, a bromine benzoindolenine-SQ has been successfully incorporated into solid lipid nanoparticles in order to overcome their solubility issues in aqueous solutions, allowing thus to enhance its spectroscopic performances with higher fluorescence quantum yield (φ_{fl}) and suggesting their potential application as PS for photodynamic anticancer treatment [33].

In this regard, although many organic nanoparticles exhibit notable advantages like high biocompatibility and bioavailability, certain issues remain, such as limited storage stability in cases like Liposomes [34,35], and relatively low cargo loading capacity [36–39] that need improvements. However, this has not been a barrier for their clinical translation, since there are different FDA-approved nanomedicines based on organic nanoparticles [40,41], highlighting lipid-based nanosystems, including COVID-19 vaccine nanoformulations [42,43]. In this challenging scenario, mesoporous silica nanoparticles (MSNs) have emerged as promising alternative nanocarriers for drug delivery. Thanks to their unique structural, textural and chemical properties and easy-to-functionalize surface, the drug loading capacity and the biocompatibility may be increased. Such advantages, together with their mechanical strength, adjustable degradability, thermal, chemical and storage stability, have significantly contributed to their progress toward forthcoming clinical translation [44–48]. In particular, since Vallet-Regí's group proposed for the first time the use of ordered mesoporous materials for drug delivery [49], MSNs have gained significant attention as versatile nanoplatform for various applications, including combined photodynamic [50,51], magnetic [52] and photothermal [53] therapies. MSNs possess a well-defined porous structure with uniform pore sizes ranging from 2 to 50 nm. This controlled porosity allows for high drug-loading capacity and controlled release kinetics, making them ideal for delivering photosensitizers. The high surface area of MSNs facilitates efficient drug loading, providing more sites for drug adsorption or encapsulation [54–56]. All these properties can help to enhance the photostability of photosensitizers, since confining the molecules within the porous structure, they are protected from external factors that may induce photobleaching or degradation. Finally, MSNs are generally considered biocompatible and well-tolerated by biological systems, reducing the risk of adverse reactions when used for drug delivery *in vivo* [51].

Herein, we propose for the first time the use of MSNs as nanocarriers of a SQ dye, specifically Br-SQ, for aPDT. This molecule was previously tested by the authors as a photosensitizer in PDT against HT-1080 cancer cells [14], showing excellent cytocompatibility up to 2 μM and demonstrating a phototoxic effect at low concentrations. Based on the excellent results obtained with cancer cells, in this work we evaluate its antibacterial properties when incorporated into MSNs. In a previous report, the authors incorporated Br-SQ into MSNs to overcome the limitation of the poor solubility and stability in an aqueous environment of this molecule, to evaluate the overall UV–Vis–NIR absorption and emission properties as well as on the PS performance *via* a combined experimental and computational physical-chemical approach [31]. In the current research, we have focused on testing the ability of Br-SQ-loaded MSNs to photoinactivate both Gram-positive *S. aureus* and Gram-negative *E. coli* bacteria, analyzing the phototoxic effect after different irradiation time and power.

2. Materials and methods

All the chemicals were purchased from Sigma Aldrich, Fluka, Merck or Riedel de Haen and were used without any further purification.

2.1. Synthesis of Br-SQ

The classic synthesis of symmetrical squarylium dyes involves the one-pot condensation of electron-rich aromatic or heterocyclic compounds with squaric acid in a solvent mixture under reflux [57]. As published by Barbero et al., SQ can be also synthesized by using a microwave synthesizer, allowing to decrease the reaction times (from hours to minutes), while increasing the SQ yield and purity [58]. The synthetic procedure followed to produce Br-SQ has been described by Serpe et al. [14]. To briefly summarize, the first step is the synthesis of the 5-bromine 2,3,3-trimethylindolium exploiting the condensation of Br-benzohydrazine with 3-methylbutan-2-one in glacial acetic acid. The second step is the quaternization of the indolenine ring with the iodobutane to obtain the quaternarized salts, while in the final step, squaric acid is overheated in a closed vessel under MW radiation in 1-butanol: toluene mixture (1:1, v/v). The characterization of the final Br-SQ as well as all the intermediate compounds agree with literature values [14,16].

2.2. Preparation of Mesoporous Silica Nanoparticles (MSNs)

MSNs with 2D hexagonal mesoporous arrangement were prepared following the modified Stöber's sol-gel process previously reported in the literature (Fig. 1) [59]. Briefly, 1 g (2.74 mmol) of cetyltrimethylammonium bromide (CTAB) was dissolved in 480 mL of

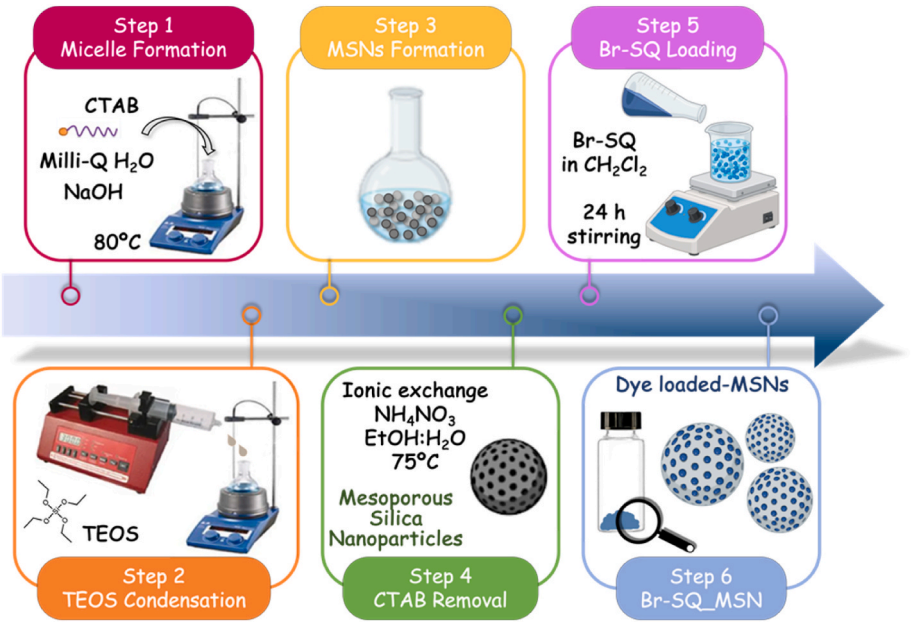

Fig. 1. Schematic setup of MSNs synthesis and Br-SQ loaded procedure.

Milli-Q water containing 3.5 mL of NaOH (2 M) in a 1 L round-bottom flask and kept in mild stirring to allow the total structure directing agent solubilization. Then, the mixture was heated at 80 °C and 5 mL (22.4 mmol) of tetraethyl orthosilicate (TEOS) were added dropwise with a pump injector NE-300 (New Era Pump systems, Inc. NY, USA) at a rate of 0.25 mL/min and was stirred for 2 h. The flask was cooled down rapidly in an ice bath and the nanoparticles were collected by centrifugation (10,000 rpm, 15 min), washed twice with Milli-Q water and twice with absolute ethanol and dried at 70 °C. 1 g of surfactant-containing MSNs was well-dispersed in 350 mL of extracting solution and the surfactant was removed by ionic exchange using 350 mL of a hydro-alcoholic (EtOH/H_2O 95:5) solution of 10 mg/L of ammonium nitrate (NH_4NO_3) at 75 °C overnight under magnetic stirring (ion exchange procedure was repeated twice). The final product was centrifuged (10,000 rpm, 15 min), washed three times with absolute ethanol and dried at 70 °C for storage.

2.3. Preparation of Br-SQ loaded MSNs

To load the Br-SQ into the pores of the MSNs, the adsorption method previously described by the authors has been followed [53] (Fig. 1). A solution of Br-SQ (8 mM) was added to a solution of MSNs (6 mg/mL) in dichloromethane (DCM) and stirred for 24 h in dark condition, to avoid the dye degradation. The suspension was then centrifuged twice at 10, 000 rpm and 10 °C for 10 min. After each cycle, the supernatant was removed and replaced with 10 mL of DCM to remove the non-loaded Br-SQ. The obtained Br-SQ loaded MSNs were finally oven-dried at 35 °C for 48 h, to remove the solvent. Sample will be hereafter named as Br-SQ_MSN.

2.4. Spectroscopic characterization of the Br-SQ and Br-SQ_MSN

UV–Vis spectroscopy. UV–Vis spectra were recorded on a Cary 300 Bio spectrophotometer (Varian, Santa Clara, CA, USA), by dissolving the free dye or the Br-SQ_MSN in different ratio of dimethyl sulfoxide (DMSO) and Phosphate Buffer Saline (PBS 50 mM, pH 7.4) in order to investigate the solubility of both the systems. UV–Vis measurements were carried out in the range of 500–800 nm and were recorded at room temperature.

2.5. Physico-chemical characterization of the Br-SQ_MSN

Transmission Electron Microscopy (TEM) and Field-Emission Scanning Electron Microscopy (FE-SEM). The mesostructure and morphology of MSN and Br-SQ_MSN samples were characterized by Transmission Electron Microscopy (TEM) and Field-Emission Scanning Electron Microscopy (FE-SEM). TEM images were recorded in a JEOL 1400 electron microscope (JEOL Ltd., Tokyo, Japan) operating at 120 kV and equipped with an CCD camera of 2048 × 2048 pixels. Sample preparation was performed by dispersing *ca.* 1 mg of sample in 2 mL of absolute ethanol, followed by sonication in a low power bath sonicator (Selecta, Spain) for 5 min and then depositing one drop of the suspension onto carbon-coated copper grids. For FE-SEM observations (TESCAN S9000G instrument), 5 mg of both MSN and Br-SQ_MSN were dispersed on a conductive carbon tape and coated with Cr layer (7 nm).

Nitrogen adsorption–desorption analysis. N_2 adsorption–desorption isotherms were measured at 77 K on a Micromeritics ASAP 2020 instrument (Micromeritics Co, Norcross, USA). Both bare MSN and Br-SQ_MSN were firstly outgassed for 24 h at 35 °C. The Brunauer-Emmett-Teller equation was applied to calculate the specific surface area (S_{BET}) from the adsorption data [60]. On the other hand, the total pore volume (V_T) was determined from the amount of N_2 adsorbed at a relative pressure of 0.95. The average mesopore diameter was obtained from the desorption branch of the isotherm by means of the Barret-Joyner-Halenda (BJH) method [61].

Thermo-Gravimetric Analysis (TG). To determine the amount of Br-SQ loaded into the MSNs, a TG of both MSN and Br-SQ_MSN was performed in a dynamic air atmosphere between 30 and 600 °C (flow rate of 100 mL/min with a heating rate of 5 °C/min) by using a Perkin-Elmer Pyris Diamond TG/DTA instrument (Perkin-Elmer, USA). The total amount of incorporated Br-SQ content was then calculated from the weight loss between 200 °C and 600 °C, subtracting the weight loss in the same range of temperature obtained for bare MSNs, ascribed to the condensation of the silanol groups on the surface.

Fourier Transform Infrared (FTIR). FTIR spectra were collected in a Nicolet Nexus spectrometer (Thermofisher Scientific, Waltham, MA) equipped with a Smart Golden Gate attenuated total reflectance (ATR) accessory (Thermo Electron Scientific Instruments LLC, Madison, WI).

Dynamic Light Scattering (DLS) and ζ-potential. Electrophoretic mobility measurements of the materials suspended in H_2O were used to

calculate the zeta-potential (ζ-potential) values of bare MSN and Br-SQ_MSN. Measurements were carried out in a Zetasizer Nano ZS (Malvern Instruments Ltd., United Kingdom) equipped with a 633 nm "red" laser. For this purpose, 1 mg of nanoparticles was added to 10 mL of Milli-Q water followed by vortex and ultrasound in a bath sonicator (Selecta, Spain) to get a homogeneous suspension. Measurements were recorded by placing *ca.* 1 mL of suspension in disposable folded capillary cells (DTS1070, Malvern Instruments). The hydrodynamic sizes (D_H) of bare MSN and Br-SQ_MSN were measured by dynamic light scattering (DLS) with the same Malvern instrument. Values presented are mean ± SD from triplicate measurements.

2.6. Evaluation of the Reactive Oxygen Species (ROS)

To evaluate the Reactive Oxygen Species (ROS) generation, 1,3-Diphenylisobenzofuran (DPBF) was selected and used as scavenger molecules, by following the protocol previously described in the literature [13,16,32]. In fact, after the reaction between DPBF and generated ROS, the colourless *o*-dibenzoylbenzene derivative is formed, allowing the monitoring of the ROS scavenger activity by following the decrease in the electronic absorption band of DBPF at 415 nm. Stock solutions of DPBF and Br-SQ were prepared in DMSO, while the stock solution of Br-SQ_MSN was prepared directly in phosphate buffer saline (PBS, 50 mM, pH 7.4). Each solution was then diluted in PBS (50 mM, pH 7.4) to obtain the final desired concentration (25 μM for DPBF, 5 μM for SQ and an amount of Br-SQ_MSN containing the same concentration of the free SQ) placed in a 1 cm quartz cell and irradiated in an aerated solar box (Solarbox 3000e, 250 W xenon lamp, CO.FO.ME.GRA) with a 250 W lamp at various time intervals. Light was filtered in an optical filter with a 515 nm cut-off, to avoid the DPBF degradation. At predefined time points, absorption spectra were recorded on a Cary 300 Bio spectrophotometer instrument. The decrease in the DBPF absorption contribution at 415 nm was plotted as a function of the irradiation time.

2.7. In vitro bacterial assay for planktonic growth inhibition

Representative Gram-positive strains (*S. aureus*, ATCC 29213) and Gram-negative strains (*E. coli*, ATCC 25922) were selected to evaluate the antimicrobial properties of both the free Br-SQ and Br-SQ_MSN systems after irradiation.

To initiate the bacterial culture, one Colony Forming Unit (CFUs) of *S. aureus* or *E. coli* was extracted and cultured in 20 mL Todd Hewitt Broth (THB) culture medium at 37 °C and under stirring conditions (100 rpm) overnight. A visible spectrophotometer (Photoanalizer D-105, Dinko instruments) was used for the determination of the working bacteria concentration. For this propose the turbidity of the inoculum was evaluated by measuring the optical density at 600 nm, OD600, firstly diluted with THB (1:6), incubated for 15 min and finally diluted at $2{\cdot}10^6$ bacteria mL^{-1} with PBSx. Br-SQ (1 mg/mL) was firstly dissolved in DMSO and then appropriately diluted in PBSx (pH 7.4) to obtain different concentrations of samples with a total amount of DMSO < 1%. On the other hand, Br-SQ_MSN and bare MSN (1 mg/mL) were directly dispersed in PBSx (pH 7.4) and diluted to the desired concentrations.

Then, 100 μL of the 1 mg/mL of Br-SQ, Br-SQ_MSN and bare MSN solutions, were placed in contact in a 96-well plate with 100 μL of the prepared of *S. aureus* or *E. coli* inoculum to obtain the final concentration of 100 nM, 500 nM, 1000 nM, 2 μM, 3 μM and 5 μM of Br-SQ (both free and incorporated into the MSN).

The bacteria culture was kept at 37 °C and under stirring conditions (100 rpm) for 2 h to allow the dye internalization. Irradiation (λ = 640 nm) was then carried out by using a compact LED array-based illumination system specifically designed and produced by Cicci Research s.r.l (Italy). This illumination system includes a RED-LED array (light source with excitation wavelength: 640 nm) composed of 96 LEDs arranged in 12 columns × 8 rows. For standard treatments, the following parameters were used: fluence 6.2 J/cm^2, irradiance 7 mW/cm^2, time 15 min and incubation time 1 h. Some treatments were also performed at higher power by setting the fluence at 15.7 J/cm^2 and irradiance at 17.4 mW/cm^2. After 1 h incubation, serial dilutions of aliquots of the treated samples were prepared and 10 μL of the final solution of each condition were seeded in Trypticase soy agar plates and cultured for 24 h at 37 °C under static conditions.

CFUs were counted after 24 h. To evaluate the potential toxicity in dark condition, the same experiments have been performed avoiding the irradiation time, maintaining the samples in dark condition. Each experimental condition was performed by triplicate in three independent experiments.

2.8. Statistical procedure

Data were reported as an average of three independent experiments with the corresponding standard deviations (±SD). Statistical analyses were performed using Student's t-test two-tailed (Excel) to determine the difference between two groups (dark *vs* light). Statistical significance values were *$p < 0.05$ (significant), **$p < 0.01$ (moderately significant), ***$p < 0.005$ (highly significant) and ****$p < 0.001$ (very highly significant).

3. Results and discussion

Pristine MSNs were synthesized by following the modified Stober's sol-gel process according to previously published protocols [44]. This method typically involves a sol-gel process, where silica precursors (TEOS) were mixed with the CTAB surfactant as structure-directing agent to create the porous structure. The mixture was aged to allow for proper pore development, and the resulting material was finally dried to obtain the pure-silica MSNs. The latter was then used for the dye loading by following the conventional impregnation method. MSNs were added to a dichloromethane solution of the Br-SQ. During the 24 h of soaking under stirring at RT the dye molecules adsorb onto the inner surfaces of the mesoporous silica. Excess or unadsorbed Br-SQ was finally removed through washing steps, obtaining the Br-SQ_MSN. Fig. 1 summarizes both procedures. Both bare MSNs and Br-SQ_MSNs in the form of dry powders have been comparatively characterized in terms of morphology, spectroscopic and chemical-physical characteristics, as well as their ability to produce reactive oxygen species before being tested for bacterial photoinactivation. The comparative characterization of pristine and Br-SQ-loaded MSNs is described in the following sections.

3.1. Physicochemical characterization of Br-SQ loaded MSNs

Field emission scanning electron microscopy (FE-SEM) images of bare MSN (Fig. S1A) showed nanoparticles with a monodispersed spherical shape with size ranging between 120 and 150 nm. The NPs size and shape of Br-SQ_MSN resulted very similar to those reported for non-loaded samples (Fig. S1B), confirming that SQ incorporation does not significantly alter the morphological features of MSNs. The characterization by TEM shows discrete nanoparticles having a spherical morphology with an average particle diameter of *ca.* 150 nm (Fig. 2A). In addition, TEM images revealed well-defined ordered pore structure with hexagonal 2D mesochannels typical of p6mm symmetry and pore diameters of approximately ~2 nm [62] according with their textural properties (see below). The comparison of TEM images before and after SQ loading demonstrated that the presence of the Br-SQ complex inside the pores of the nanoparticles did not modify neither the nanoparticle morphology nor the 2D hexagonal symmetry. An enlargement of the marked areas in Fig. 2B shows the mesoporous order observed in both projections, perpendicular and parallel to the mesoporous channels.

Additionally, the presence of SQ complex into MSNs was confirmed by FTIR studies. To these aim the FTIR spectra of pure Br-SQ, pristine MSN and dye-loaded Br-SQ_MSN were recorded (Fig. 3A). FTIR spectrum of pure Br-SQ shows characteristic vibration bands at *ca.* 2948 and

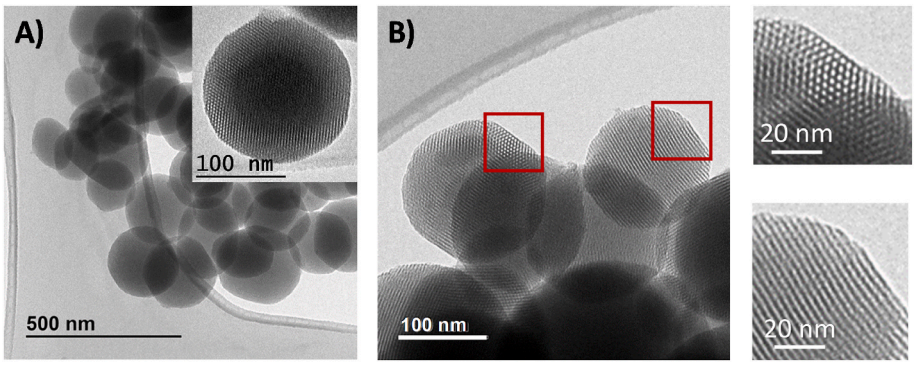

Fig. 2. TEM images of A) unloaded and B) Br-SQ loaded MSNs. An enlargement of the marked areas is shown where the mesoporous order is observed.

2860 cm^{-1} assigned to ν(C–H) of aliphatic –CH_2– chains; an intense band at 1610 cm^{-1} assigned to C═O stretching mode; two bands at 1345 and 1165 cm^{-1} which were attributed to C–O^- stretching modes; and two bands at 1500 and 1450 cm^{-1} that were ascribed to C–N stretching modes. In addition, vibrations bands were also observed in the 1075 to 1000 cm^{-1} range which were attributed to the presence of aromatic ring bending modes, while at 660-560 cm^{-1} the bands were related to C–Br stretching modes. In the case of FTIR spectra of both pristine MSN and dye-loaded Br-SQ_MSN samples the characteristic vibration bands associated to the silica network were observed, namely the stretching vibration of H-bonded hydroxyls in the 3750–3000 cm^{-1} range, Si–O stretching vibrations at *ca.* 1040 and 790 cm^{-1}, and the Si–O–Si strength at 430 cm^{-1}. Additional signals corresponding to the Br-SQ dye presence compared to pristine MSN sample were observed in the Br-SQ_MSN spectrum. Novel bands at 2985 and 2900 cm^{-1} assigned to ν(C–H) of aliphatic were observed; at 1630 cm^{-1} assigned to C═O stretching mode; two signals at 1393 and 1290 cm^{-1} attributed to C–O^- stretching modes; and two bands at 1498 and 1452 cm^{-1} ascribed to C–N stretching modes. These findings point to the successful incorporation of the Br-SQ dye into the MSNs, as it is confirmed by N_2 adsorption and thermogravimetric measurements (*vide infra*).

N_2 sorption porosimetry measurements provided information about the textural properties of MSNs before and after being loaded with Br-SQ. The main parameters are listed in Table 1 and Fig. 3B shows the N_2 adsorption isotherms and mesopore size distributions (inset). Both isotherms are type IV according to the IUPAC classification, which are characteristic of mesoporous materials exhibiting typical of MCM-41 type mesoporous materials with parallel cylindrical pores [63]. After being loaded with Br-SQ, MSNs showed a reduction of the total pore volume (V_T) from 0.86 cm^3/g to 0.66 cm^3/g, whereas the surface area (S_{BET}) experienced a reduction from 1038 m^2/g to 826 m^2/g. The decrease in these textural parameters as a consequence of the loading process constitute indirect evidence of the efficient confinement of the Br-SQ molecules into the mesoporous cavities. It is worth mentioning that there is remaining surface area and empty pore volume available to incorporate other antimicrobial agents for synergistic bactericidal effects, which would be an additional advantage when using these mesoporous nanocarriers.

Br-SQ loading in MSNs was carried out by the impregnation method in dichloromethane solvent, and total amount of Br-SQ loaded was determined by thermogravimetric (TG) analysis subtracting the data obtained for the loaded and unloaded samples (Fig. 3C). Using TG curve for bare MSN, as a reference, a first weight loss corresponding to *ca.* 2.5% was observed at about 100–110 °C, which can be assigned to water desorption. The weight was then kept constant up to 250–280 °C, and from this temperature a weight loss of about 6% occurred, which can be associated with polycondensation of remaining ethoxy and silanol groups from non-hydrolized alkoxysilane groups. The Br-SQ_MSN thermogram showed a noticeable weight decrease between 250 °C and 600 °C, attributed not only to the Si–OEt and Si–OH polycondensation, but mainly to the loss of Br-SQ incorporated within the MSN pores (Br-SQ thermogram, inset Fig. 3C, showed that from 500 °C all organic matter has been removed). This difference in percentage weight reduction was considered to calculate the amount of the loaded SQ through multiple intermolecular interactions (*e.g.*, hydrogen bonding, dispersive forces). Similar interactions have been reported in the literature for other drugs incorporated into mesoporous materials [62, 64–66]. According to the TG analysis, the weight percentage of Br-SQ loaded into MSN was determined to be ~7.5% (w/w). This value is higher than that previously reported [31], which is expected to provide the nanosystems of improved antimicrobial effect.

The hydrodynamic diameters (D_H) of the pure-silica MSN and Br-SQ_MSN samples were measured by dynamic light scattering (DLS) in water medium, displaying good dispersions with a narrow size distribution for both samples. The D_H of the nanoparticles (Table 1) was found to be 155 nm for MSN and 175 nm for Br-SQ_MSN, which, as expected, are slightly larger than those estimated from SEM/TEM images. Table 1 includes the ζ-potential values of both samples, with very similar behavior. These values are due to deprotonation of silanol groups on the MSN surface (R-Si-OH + H_2O ⇌ R–SiO^- + H_3O^+), and the presence of Br-SQ in the mesopores did not affect the surface charge of the Br-SQ_MSN nanosystem.

3.2. Spectroscopic characterization of Br-SQ loaded MSNs

The spectroscopic absorption of free dye Br-SQ and Br-SQ_MSN were evaluated in order to investigate the difference in aqueous media solubility. As shown in Fig. 4A, the absorption spectrum of Br-SQ in 100% DMSO shows an intense absorption peak typical of SQ dyes, with a maximum absorption at 652 nm. However, by increasing the percentage of PBS the absorption maximum gradually decreases with a simultaneous hypsochromic shift. At the same time, the hypsochromic shoulder increases in intensity evidencing the formation of aggregates. When the percentage of PBS exceeds 50%, the SQ-like shape of the absorption spectrum is missing while at 100% PBS there is no dissolution of the Br-SQ leading to a complete loss of the spectroscopic properties typically observed in organic solvents. On the other hand, when Br-SQ is incorporated inside MSN the solubility in aqueous media increases as shown in Fig. 4B. The shape of the absorption spectrum slightly changes compared to free Br-SQ in DMSO due to some scattering of particles in the suspension.

3.3. ROS measurement analysis in vitro

An initial assessment of the Br-SQ_MSN capability to generate ROS was conducted using 1,3-diphenylisobenzofuran (DPBF) as a probe. DPBF rapidly reacts with ROS and singlet oxygen [67,68] produced by the photosensitizers (PSs) after the irradiation, resulting in the formation of a colorless o-dibenzoylbenzene derivative, which is characterized by the disappearance of DPBF's characteristic absorption band at 415

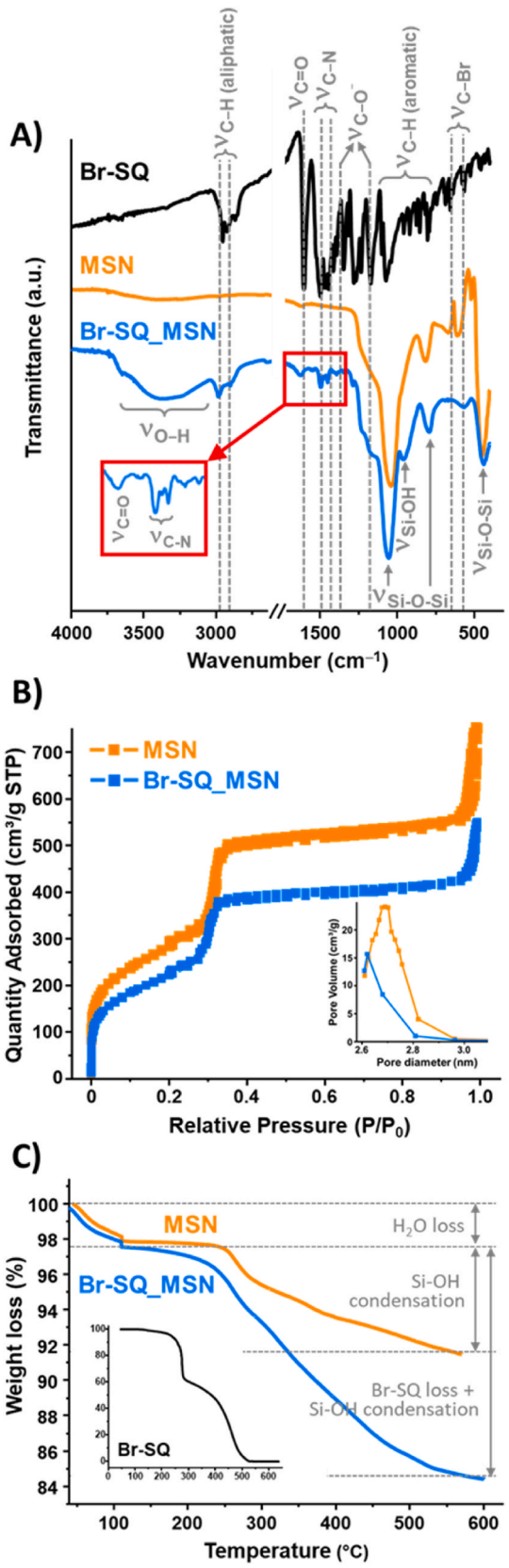

Fig. 3. A) FTIR spectra, B) N_2 adsorption-desorption isotherms and pore size distributions (inset), and C) thermograms of Br-SQ, unloaded MSN and Br-SQ_MSN samples.

nm. To evaluate the efficacy of the Br-SQ_MSN, the reduction in DPBF's absorption band at 415 nm over irradiation time was compared to values obtained by irradiating the free Br-SQ already reported in literature [14]. As shown in Fig. 5, empty MSNs exhibited a slight ability to generate ROS. In fact, considering the difference in the rate of ROS production in the whole experiment, the contribution of ROS production by MSNs alone can be considered negligible. The decrease in DPBF absorbance in the presence of MSNs alone may not be due to ROS production by the latter but can be ascribed to a gradual degradation of DPBF itself following repeated irradiations. On the other hand, Br-SQ_MSN demonstrated a reduced capacity for ROS production compared to the free dye, probably due to light scattering phenomena. In fact, the presence of MSNs can scatter light, preventing the light to reach and excite the dye incorporated within the mesopores, leading to a decreased ROS production.

It is important to highlight that the assessment of ROS production is conducted under distinct conditions for Br-SQ_MSN and the free dye. Specifically, the Br-SQ_MSN are evaluated in 100% PBS, while the free dye necessitates dissolution in 100% DMSO, followed by dilutions in PBS to achieve a final DMSO concentration below 1%.

3.4. *In vitro antimicrobial PDT*

The antimicrobial photodynamic effect of free Br-SQ and Br-SQ_MSN was investigated against both representative Gram-positive *S. aureus* and Gram-negative *E. coli* bacteria strains by evaluating different dye concentration, irradiation time, and irradiation power. As initial trial, aPDT treatment parameters were established based on previous studies conducted on cancer cell lines [14,16,32]. These parameters included a Br-SQ concentration range from 100 nM to 1 μM in PBSx buffer at pH 7.4, an irradiation time of 15 min, irradiation power at 640 nm with a fluence of 6.2 J/cm^2, and irradiance of 7 mW/cm^2. As depicted in Fig. 6, as far as the antimicrobial effect on *S. aureus* is concerned, the free dye exhibited minimal toxicity in dark conditions but demonstrated potent bacterial inactivation after irradiation at all tested concentrations. The unloaded MSNs do not appear to have a significant effect on bacterial viability, as previously demonstrated by the authors [62,69,70], both in the dark and after irradiation. On the other hand, MSN loaded with Br-SQ exhibited negligible toxicity in dark conditions but displayed potent phototoxicity after irradiation, already at the lowest concentration of 100 nM.

Conversely, after the application of the same protocol to *E. coli* strain, any significant effect from either the free Br-SQ or the Br-SQ_MSN has been observed after irradiation (Fig. S2). This difference in response between the two bacterial strains may be ascribed to the variance in their cell membrane permeability [71]. *E. coli*, being a Gram-negative bacterium, has an outer membrane that acts as an additional barrier, which might hinder the penetration of the antimicrobial agents. Moreover, the presence of MSNs can scatter the light or absorb part of the light thus limiting the light dose able to reach and excite the dye and the following ROS production, as already observed in Fig. 5. This difference does not appear to be significant for *S. aureus*, possibly due to the molecule and nanoparticles' greater affinity for the membranes of Gram-positive bacteria. In fact, usually, Gram-positive bacteria are more susceptible to neutral and anionic PS, while Gram-negative ones showed more resistance due to the additional asymmetric outer membrane composed by numerous strongly negatively charged molecules [71].

These results highlighted the importance of considering the specific properties and structures of the targeted bacteria when developing and evaluating antimicrobial agents for aPDT. Since also the applied treatments can significantly influence the effectiveness of the therapy, we decided to increase both the dye concentration (2, 3, and 5 μM) as well as the treatment time (from 15 to 30 min) with irradiation power at 640 nm, fluence of 12.5 J/cm^2, and irradiance of 7 mW/cm^2.

Unfortunately, as shown from Fig. S3, neither an increase in concentration nor an extension of the irradiation time appear to have any

Table 1
Textural and physicochemical properties of MSN and Br-SQ_MSN samples.

	S_{BET}[a] (m^2/g)	V_T[b] (cm^3/g)	D_P[c] (nm)	Org. cont. (%wt)[d]	D_H (nm)[e] (% population)	ζ-potential[f] (mV)
MSN	1038	0.86	2.69	~8.0	155.2 ± 20.5 (27.8%)	−24.2 ± 0.7
Br-SQ_MSN	826	0.66	2.62	~15.5	175.6 ± 36.1 (19.3%)	−22.0 ± 0.8

[a] Specific surface area obtained by using BET equation.
[b] Total pore volume obtained at $P/P_0 = 0.95$.
[c] Average pore diameter calculated by using the BJH method.
[d] The organic content is determined from the TGA weight losses, excluding the weight loss due to the desorption of water (up to 150 °C) and further corrected by the weight loss of the surfactant extracted unmodified MSNs.
[e] Hydrodynamic diameter.
[f] ζ-potential values determined in water medium.

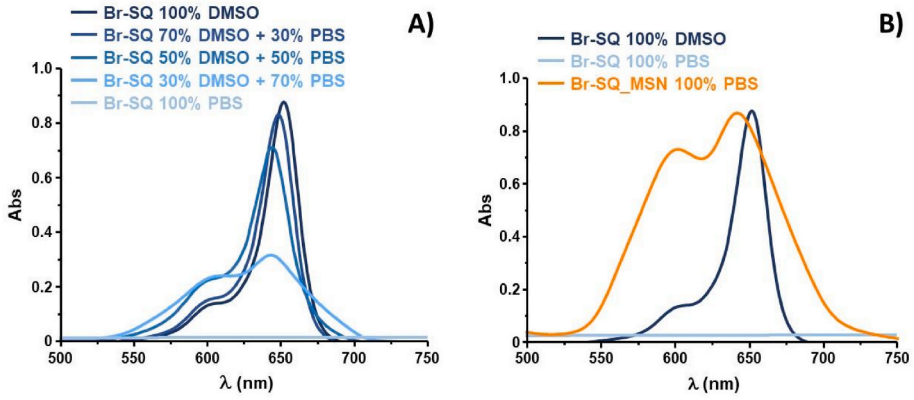

Fig. 4. A) UV–Vis spectra of Br-SQ dissolved in different percentages of DMSO and PBS, B) Comparison of the UV–Vis spectra of free Br-SQ in 100% DMSO, 100% PBS and Br-SQ-MSN in 100% PBS. The concentration of Br-SQ was kept constant for all the measurements.

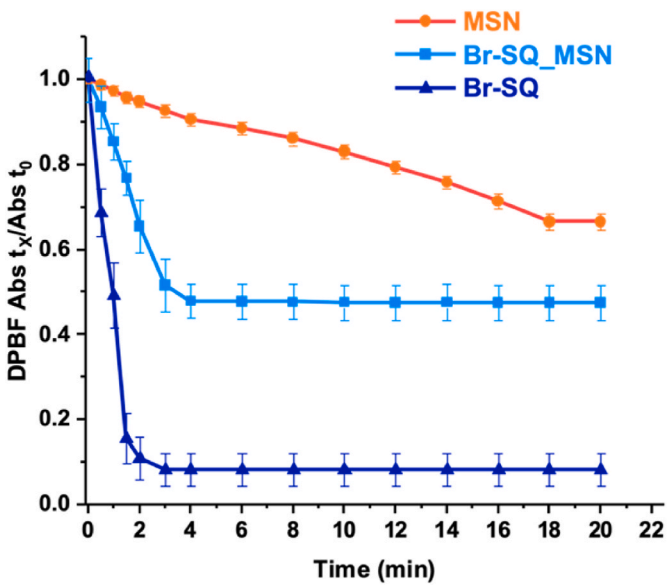

Fig. 5. Decay of the absorption band of DPBF at 415 nm as a function of the irradiation time in the presence of free Br-SQ, MSN and Br-SQ_MSN.

effect on the bacterial viability of *Escherichia coli*. In fact, no differences in viability after irradiation are observable compared to the dark conditions. Furthermore, higher dye concentrations seem to notably increase the dark toxicity (50% viability).

Since this limited effect appears to be related to both membrane permeability issues and light scattering, we decided to increase the available light dosage to excite the dye, moving from a fluence of 12.5 J/cm^2 to 15.7 J/cm^2. In this case, the higher light dosage seems to have an impact both on the Br-SQ alone and the Br-SQ incorporated into the MSN (Fig. 7). In fact, the Br-SQ alone exhibits phototoxicity at all tested concentrations, with a gradual increase in dark toxicity at higher dye concentrations (3 and 5 μM). The same effect can be observed for Br-SQ_MSN, where concentrations of 100 nM, 500 nM, and 1 μM show excellent bacterial viability in dark conditions and a remarkable phototoxic effect after irradiation. The phototoxic effect is also visible at higher concentrations, where, however, the dark toxicity also increases.

It is important to note that the concentrations used to achieve an aPDT effect with Br-SQ_MSN are significantly lower compared to the concentrations of photosensitizers typically used in aPDT, which are often in the μM range. For example, the well-known methylene blue is reported to be effective at concentrations greater than 40 μM, while toluidine blue O is effective at concentrations exceeding 10 μM [72,73]. Specifically, as reported by Serpe et al. [14], Br-SQ is cytocompatible on HT-1080 cells up to 2 μM and it is phototoxic at concentration of 1 μM, which is 10 times lower compared to the concentration used to observe a photodamage against bacteria. This means that Br-SQ_MSN can be used for bacterial photoinactivation without any toxic effect against healthy cells, thus preserving the functionality of nearby tissues. Moreover, in the perspective of possible future applications, the use of low concentration allows for more efficiency and cost-effectiveness with potential benefits in terms of optimization of pharmacokinetics, reduction of side effects, and reduction of the cost of phototherapy. The results presented in this study demonstrate how the use of Br-SQ allows for the reduction of PS concentrations, thereby minimizing potential toxicity and side effects (*e.g.,* post exposure light sensitivity).

4. Conclusions

In this study, a bromine-substituted indolenine-based SQ (Br-SQ),

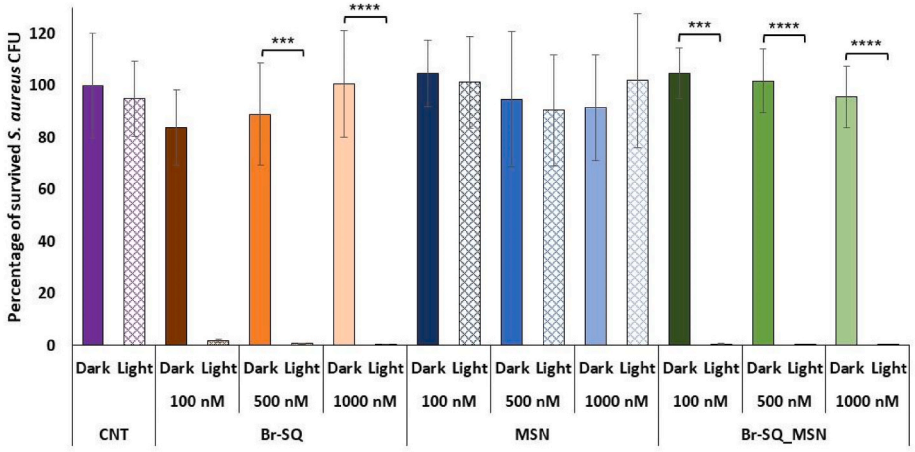

Fig. 6. *In vitro* antimicrobial effect of different concentrations of Br-SQ, MSN and Br-SQ_MSN on *S. aureus* in the dark and after irradiation (640 nm LED, fluence 6.2 J/cm^2, irradiance 7 mW/cm^2 for 15 min). For Br-SQ_MSN the concentrations refer to dyes incorporated into MSNs (from 100 nM to 1μ M) in PBS buffer, pH 7.4. Data are reported as an average of three independent experiments. p values: ***$p < 0.005$ and ****$p < 0.001$.

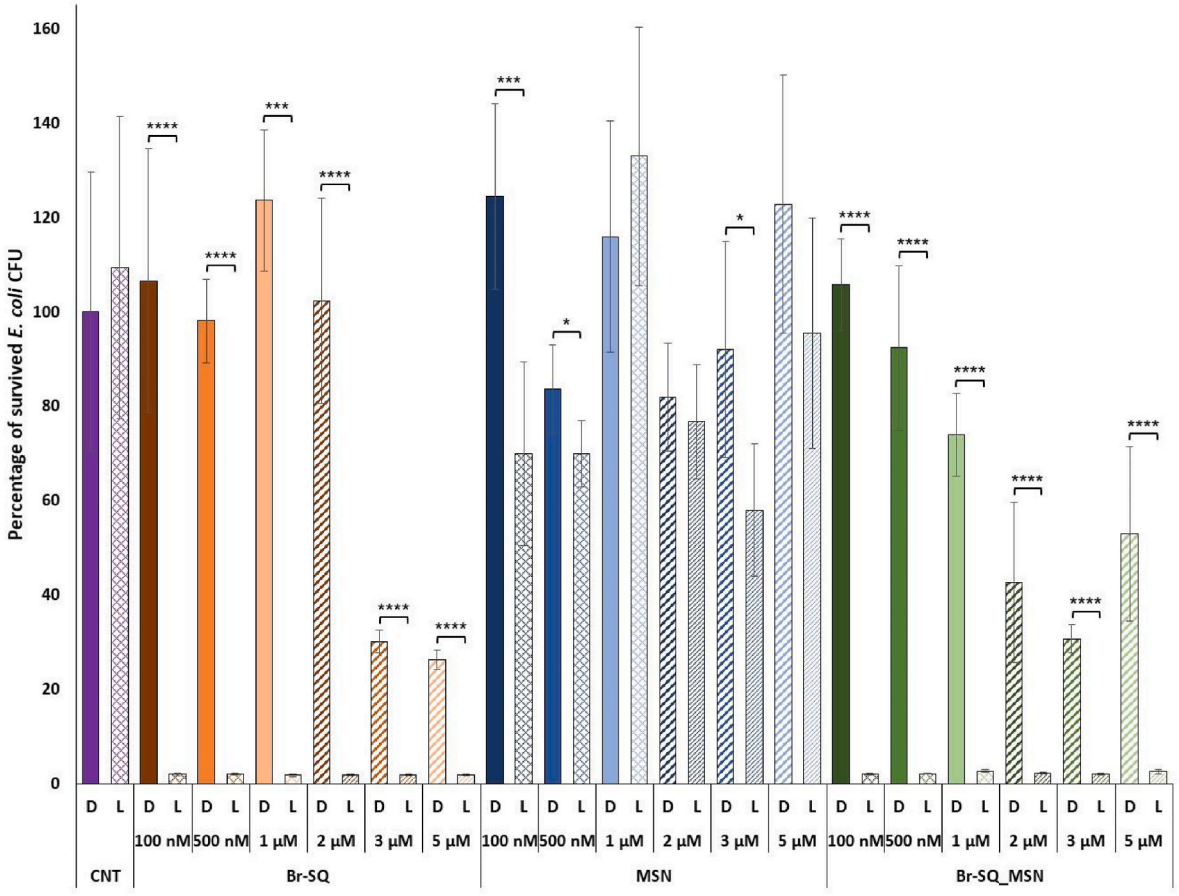

Fig. 7. *In vitro* antimicrobial effect of different concentrations of Br-SQ, MSN and Br-SQ_MSN on *E. coli* in the dark and after irradiation (640 nm LED, Fluence 15.7 J/cm^2, Irradiance 17.4 mW/cm^2 for 15 min). For Br-SQ_MSN the concentrations refer to dyes incorporated into MSNs (from 100 nM to 5 μM) in PBS buffer, pH 7.4. Data are reported as an average of three independent experiments. p values: *$p < 0.05$, ***$p < 0.005$ and ****$p < 0.001$.

initially recognized for its efficacy in Photodynamic Therapy (PDT) against specific tumor cell lines, was explored for its potential in antimicrobial Photodynamic Therapy (aPDT). Br-SQ was incorporated into mesoporous silica nanoparticles (MSNs) to increase its solubility and limit its tendency to form aggregates in physiological conditions. Detailed characterization reveals a well-defined spherical nanosystem with a size range of 120–150 nm, maintaining the ordered pore structure. The hydrodynamic particle diameter and ζ-potential are found to be suitable for the intended application. Textural analysis indicates a reduction in surface area and pore volume after loading Br-SQ into MSNs, confirming efficient confinement within mesoporous cavities. The weight percentage of Br-SQ loaded into MSNs was determined to be approximately 7.5% (w/w) based on TG analysis. Despite a reduced capacity for ROS production in Br-SQ-loaded MSNs compared to the free

dye, antimicrobial effects are observed against both Gram-positive *S. aureus* and Gram-negative *E. coli* bacteria. Notably, the aPDT effect is more pronounced against *S. aureus* at a lower dye concentration and minimum irradiation power, while *E. coli* exhibits higher resistance, potentially attributed to differences in cell membrane permeability. In both cases, the concentrations used to achieve an aPDT effect with Br-SQ_MSN are significantly lower (100 nM) compared to the concentrations of photosensitizers typically used in aPDT, which are often in the μM range.

The use of lower concentrations of Br-SQ_MSN for achieving an aPDT effect represents a significant advancement in the field of aPDT opening up avenues for more efficient, cost-effective, and targeted treatments with potential benefits in terms of safety and biocompatibility. Albeit, further research and both *in vitro* and *in vivo* validation is needed, these findings open up new opportunities in the management of infection using antibiotic-free nanoformulations with antimicrobial effect for diverse clinical scenarios.

CRediT authorship contribution statement

Degnet Melese Dereje: Writing – original draft, Methodology, Data curation. **Ana García:** Writing – review & editing, Writing – original draft, Methodology, Data curation, Conceptualization. **Carlotta Pontremoli:** Writing – review & editing, Supervision, Methodology, Data curation, Conceptualization. **Blanca González:** Writing – review & editing, Validation, Formal analysis. **Montserrat Colilla:** Writing – review & editing, Validation, Formal analysis. **María Vallet-Regí:** Funding acquisition. **Isabel Izquierdo-Barba:** Writing – review & editing, Funding acquisition, Conceptualization. **Nadia Barbero:** Writing – review & editing, Supervision, Funding acquisition, Conceptualization.

Declaration of competing interest

The authors declare that they have no known competing financial interests or personal relationships that could have appeared to influence the work reported in this paper.

Data availability

Data will be made available on request.

Acknowledgements

D.M.D, C.P. and N.B. acknowledge support from the Project CH4.0 under the MUR program “Dipartimenti di Eccellenza 2023–2027" (CUP: D13C22003520001) and “Grant for Internalization (GFI)”, granted by Department of Chemistry, University of Torino, Italy.

A.G., B.G., M.C., M.V.R. and I.I.B. thank the Spanish Government, Ministerio de Ciencia e Innovación, (projects PID2020-117091RB-I00 (NANONICHE) and PID2019-106436RB-I00 (iBONE)), the European Research Council ERC-2015-AdG (VERDI) grant No. 694160 and the Fundación Ramón Areces (FD5/22_01, Nano4Infection) for their support.

Appendix A. Supplementary data

Supplementary data to this article can be found online at https://doi.org/10.1016/j.micromeso.2024.113096.

References

[1] C.J.L. Murray, K.S. Ikuta, F. Sharara, L. Swetschinski, G. Robles Aguilar, A. Gray, C. Han, C. Bisignano, P. Rao, E. Wool, S.C. Johnson, A.J. Browne, M.G. Chipeta, F. Fell, S. Hackett, G. Haines-Woodhouse, B.H. Kashef Hamadani, E.A.P. Kumaran, B. McManigal, S. Achalapong, R. Agarwal, S. Akech, S. Albertson, J. Amuasi, J. Andrews, A. Aravkin, E. Ashley, F.-X. Babin, F. Bailey, S. Baker, B. Basnyat, A. Bekker, R. Bender, J.A. Berkley, A. Bethou, J. Bielicki, S. Boonkasidecha, J. Bukosia, C. Carvalheiro, C. Castañeda-Orjuela, V. Chansamouth, S. Chaurasia, S. Chiurchiù, F. Chowdhury, R. Clotaire Donatien, A.J. Cook, B. Cooper, T. R. Cressey, E. Criollo-Mora, M. Cunningham, S. Darboe, N.P.J. Day, M. De Luca, K. Dokova, A. Dramowski, S.J. Dunachie, T. Duong Bich, T. Eckmanns, D. Eibach, A. Emami, N. Feasey, N. Fisher-Pearson, K. Forrest, C. Garcia, D. Garrett, P. Gastmeier, A.Z. Giref, R.C. Greer, V. Gupta, S. Haller, A. Haselbeck, S.I. Hay, M. Holm, S. Hopkins, Y. Hsia, K.C. Iregbu, J. Jacobs, D. Jarovsky, F. Javanmardi, A. W.J. Jenney, M. Khorana, S. Khusuwan, N. Kissoon, E. Kobeissi, T. Kostyanev, F. Krapp, R. Krumkamp, A. Kumar, H.H. Kyu, C. Lim, K. Lim, D. Limmathurotsakul, M.J. Loftus, M. Lunn, J. Ma, A. Manoharan, F. Marks, J. May, M. Mayxay, N. Mturi, T. Munera-Huertas, P. Musicha, L.A. Musila, M.M. Mussi-Pinhata, R.N. Naidu, T. Nakamura, R. Nanavati, S. Nangia, P. Newton, C. Ngoun, A. Novotney, D. Nwakanma, C.W. Obiero, T.J. Ochoa, A. Olivas-Martinez, P. Olliaro, E. Ooko, E. Ortiz-Brizuela, P. Ounchanum, G.D. Pak, J.L. Paredes, A.Y. Peleg, C. Perrone, T. Phe, K. Phommasone, N. Plakkal, A. Ponce-de-Leon, M. Raad, T. Ramdin, S. Rattanavong, A. Riddell, T. Roberts, J.V. Robotham, A. Roca, V.D. Rosenthal, K. E. Rudd, N. Russell, H.S. Sader, W. Saengchan, J. Schnall, J.A.G. Scott, S. Seekaew, M. Sharland, M. Shivamallappa, J. Sifuentes-Osornio, A.J. Simpson, N. Steenkeste, A.J. Stewardson, T. Stoeva, N. Tasak, A. Thaiprakong, G. Thwaites, C. Tigoi, C. Turner, P. Turner, H.R. van Doorn, S. Velaphi, A. Vongpradith, M. Vongsouvath, H. Vu, T. Walsh, J.L. Walson, S. Waner, T. Wangrangsimakul, P. Wannapinij, T. Wozniak, T.E.M.W. Young Sharma, K.C. Yu, P. Zheng, B. Sartorius, A.D. Lopez, A. Stergachis, C. Moore, C. Dolecek, M. Naghavi, Global burden of bacterial antimicrobial resistance in 2019: a systematic analysis, Lancet 399 (2022) 629–655, https://doi.org/10.1016/S0140-6736(21)02724-0.

[2] J. Conly, B. Johnston, Where are all the new antibiotics? The new antibiotic paradox, Can. J. Infect Dis. Med. Microbiol. 16 (2005) 159–160, https://doi.org/10.1155/2005/892058.

[3] J. Davies, D. Davies, Origins and evolution of antibiotic resistance, Microbiol. Mol. Biol. Rev. 74 (2010) 417–433, https://doi.org/10.1128/MMBR.00016-10.

[4] F. Cieplik, D. Deng, W. Crielaard, W. Buchalla, E. Hellwig, A. Al-Ahmad, T. Maisch, Antimicrobial photodynamic therapy – what we know and what we don't, Crit. Rev. Microbiol. 44 (2018) 571–589, https://doi.org/10.1080/1040841X.2018.1467876.

[5] F. Cieplik, W. Buchalla, E. Hellwig, A. Al-Ahmad, K.A. Hiller, T. Maisch, L. Karygianni, Antimicrobial photodynamic therapy as an adjunct for treatment of deep carious lesions—a systematic review, Photodiagnosis Photodyn. Ther. 18 (2017) 54–62, https://doi.org/10.1016/j.pdpdt.2017.01.005.

[6] F. Nakonechny, M.A. Firer, Y. Nitzan, M. Nisnevitch, Intracellular antimicrobial photodynamic therapy: a novel technique for efficient eradication of pathogenic bacteria, Photochem. Photobiol. 86 (2010) 1350–1355, https://doi.org/10.1111/j.1751-1097.2010.00804.x.

[7] H. Mahmoudi, A. Bahador, M. Pourhajibagher, M.Y. Alikhani, Antimicrobial photodynamic therapy: an effective alternative approach to control bacterial infections, J. Laser Med. Sci. 9 (2018) 154–160, https://doi.org/10.15171/jlms.2018.29.

[8] A.S. Garcez, M. Kaplan, G.J. Jensen, F.R. Scheidt, E.M. Oliveira, S.S. Suzuki, Effects of antimicrobial photodynamic therapy on antibiotic-resistant Escherichia coli, Photodiagnosis Photodyn. Ther. 32 (2020) 102029, https://doi.org/10.1016/j.pdpdt.2020.102029.

[9] F. Ramos-Martín, N. D'Amelio, Drug resistance: an incessant fight against evolutionary strategies of survival, Microbiol. Res. 14 (2023) 507–542, https://doi.org/10.3390/microbiolres14020037.

[10] X. Pang, D. Li, J. Zhu, J. Cheng, G. Liu, Beyond antibiotics: photo/sonodynamic approaches for bacterial theranostics, Nano-Micro Lett. 12 (2020) 144, https://doi.org/10.1007/s40820-020-00485-3.

[11] Y. Liu, R. Qin, S.A.J. Zaat, E. Breukink, M. Heger, Antibacterial photodynamic therapy: overview of a promising approach to fight antibiotic-resistant bacterial infections, J Clin Transl Res 1 (2015) 140–167.

[12] J. Ghorbani, D. Rahban, S. Aghamiri, A. Teymouri, A. Bahador, Photosensitizers in antibacterial photodynamic therapy: an overview, Laser Ther. 27 (2018) 293–302, https://doi.org/10.5978/islsm.27_18-RA-01.

[13] B. Ciubini, S. Visentin, L. Serpe, R. Canaparo, A. Fin, N. Barbero, Design and synthesis of symmetrical pentamethine cyanine dyes as NIR photosensitizers for PDT, Dyes Pigments 160 (2019) 806–813, https://doi.org/10.1016/j.dyepig.2018.09.009.

[14] L. Serpe, S. Ellena, N. Barbero, F. Foglietta, F. Prandini, M.P. Gallo, R. Levi, C. Barolo, R. Canaparo, S. Visentin, Squaraines bearing halogenated moieties as anticancer photosensitizers: synthesis, characterization and biological evaluation, Eur. J. Med. Chem. 113 (2016) 187–197, https://doi.org/10.1016/j.ejmech.2016.02.035.

[15] D.M. Dereje, C. Pontremoli, M.J. Moran Plata, S. Visentin, N. Barbero, Polymethine dyes for PDT: recent advances and perspectives to drive future applications, Photochem. Photobiol. Sci. 21 (2022) 397–419, https://doi.org/10.1007/s43630-022-00175-6.

[16] C. Pontremoli, G. Chinigò, S. Galliano, M.J. Moran Plata, D.M. Dereje, E. Sansone, A. Gilardino, C. Barolo, A. Fiorio Pla, S. Visentin, N. Barbero, Photosensitizers for photodynamic therapy: structure-activity analysis of cyanine dyes through design of experiments, Dyes Pigments 210 (2023) 111047, https://doi.org/10.1016/j.dyepig.2022.111047.

[17] C. Butnarasu, N. Barbero, C. Barolo, S. Visentin, Interaction of squaraine dyes with proteins: looking for more efficient fluorescent turn-on probes, Dyes Pigments 184 (2021) 108873, https://doi.org/10.1016/j.dyepig.2020.108873.

[18] C. Butnarasu, N. Barbero, C. Barolo, S. Visentin, Squaraine dyes as fluorescent turn-on sensors for the detection of porcine gastric mucin: a spectroscopic and kinetic

study, J. Photochem. Photobiol., B 205 (2020) 111838, https://doi.org/10.1016/j.jphotobiol.2020.111838.
[19] C. Butnarasu, C. Pontremoli, M.J. Moran Plata, N. Barbero, S. Visentin, Squaraine dyes as fluorescent turn-on probes for mucins: a step toward selectivity, Photochem. Photobiol. 99 (2023) 562–569, https://doi.org/10.1111/php.13722.
[20] C. Yang, W. Sheng, M. Moemeni, M. Bates, C.K. Herrera, B. Borhan, R.R. Lunt, Ultraviolet and near-infrared dual-band selective-harvesting transparent luminescent solar concentrators, Adv. Energy Mater. 11 (2021), https://doi.org/10.1002/aenm.202003581.
[21] J. He, Y.J. Jo, X. Sun, W. Qiao, J. Ok, T. il Kim, Z. Li, Squaraine dyes for photovoltaic and biomedical applications, Adv. Funct. Mater. 31 (2021) 1–35, https://doi.org/10.1002/adfm.202008201.
[22] D. Saccone, S. Galliano, N. Barbero, P. Quagliotto, G. Viscardi, C. Barolo, Polymethine dyes in hybrid photovoltaics: structure-properties relationships, Eur. J. Org Chem. 2016 (2016) 2244–2259, https://doi.org/10.1002/ejoc.201501598.
[23] R.R. Avirah, D.T. Jayaram, N. Adarsh, D. Ramaiah, Squaraine dyes in PDT: from basic design to in vivo demonstration, Org. Biomol. Chem. 10 (2012) 911–920, https://doi.org/10.1039/c1ob06588b.
[24] D. Bagchi, A. Bhattacharya, T. Dutta, S. Nag, D. Wulferding, P. Lemmens, S.K. Pal, Nano MOF entrapping hydrophobic photosensitizer for dual-stimuli-responsive unprecedented therapeutic action against drug-resistant bacteria, ACS Appl. Bio Mater. 2 (2019) 1772–1780, https://doi.org/10.1021/acsabm.9b00223.
[25] Ferdinandus, C. Joo, D. Kai, C.-L.K. Lee, Synergistic antibacterial action of lignin-squaraine hybrid photodynamic therapy: advancing towards effective treatment of antibiotic-resistant bacteria, J. Mater. Chem. B 11 (2023) 5748–5751, https://doi.org/10.1039/D3TB00629H.
[26] D. Ramaiah, I. Eckert, K.T. Arun, L. Weidenfeller, B. Epe, Squaraine dyes for photodynamic therapy: study of their cytotoxicity and genotoxicity in bacteria and mammalian cells, Photochem. Photobiol. 76 (2002) 561–703, https://doi.org/10.1562/0031-8655(2002)0760672SDFPTS2.0.CO2.
[27] D. Bagchi, V.S.S. Rathnam, P. Lemmens, I. Banerjee, S.K. Pal, NIR-Light-Active ZnO-based nanohybrids for bacterial biofilm treatment, ACS Omega 3 (2018) 10877–10885, https://doi.org/10.1021/acsomega.8b00716.
[28] D. Bechet, P. Couleaud, C. Frochot, M.-L. Viriot, F. Guillemin, M. Barberi-Heyob, Nanoparticles as vehicles for delivery of photodynamic therapy agents, Trends Biotechnol. 26 (2008) 612–621, https://doi.org/10.1016/j.tibtech.2008.07.007.
[29] J. Song, J. Qu, M.T. Swihart, P.N. Prasad, Near-IR responsive nanostructures for nanobiophotonics: emerging impacts on nanomedicine, Nanomedicine 12 (2016) 771–788, https://doi.org/10.1016/j.nano.2015.11.009.
[30] L. Jiao, Y. Liu, X. Zhang, G. Hong, J. Zheng, J. Cui, X. Peng, F. Song, Constructing a local hydrophobic cage in dye-doped fluorescent silica nanoparticles to enhance the photophysical properties, ACS Cent. Sci. 6 (2020) 747–759, https://doi.org/10.1021/acscentsci.0c00071.
[31] I. Miletto, A. Fraccarollo, N. Barbero, C. Barolo, M. Cossi, L. Marchese, E. Gianotti, Mesoporous silica nanoparticles incorporating squaraine-based photosensitizers: a combined experimental and computational approach, Dalton Trans. 47 (2018) 3038–3046, https://doi.org/10.1039/c7dt03735j.
[32] N. Bordignon, M. Köber, G. Chinigò, C. Pontremoli, E. Sansone, G. Vargas-Nadal, M.J. Moran Plata, A. Fiorio Pla, N. Barbero, J. Morla-Folch, N. Ventosa, Quatsomes loaded with squaraine dye as an effective photosensitizer for photodynamic therapy, Pharmaceutics 15 (2023) 902, https://doi.org/10.3390/pharmaceutics15030902.
[33] G. Chinigò, A. Gonzalez-Paredes, A. Gilardino, N. Barbero, C. Barolo, P. Gasco, A. Fiorio Pla, S. Visentin, Polymethine dyes-loaded solid lipid nanoparticles (SLN) as promising photosensitizers for biomedical applications, Spectrochim. Acta Mol. Biomol. Spectrosc. 271 (2022) 120909, https://doi.org/10.1016/j.saa.2022.120909.
[34] Y. Peng, J. Bariwal, V. Kumar, C. Tan, R.I. Mahato, Organic nanocarriers for delivery and targeting of therapeutic agents for cancer treatment, Adv. Ther. 3 (2020), https://doi.org/10.1002/adtp.201900136.
[35] J.F. Coelho, P.C. Ferreira, P. Alves, R. Cordeiro, A.C. Fonseca, J.R. Góis, M.H. Gil, Drug delivery systems: advanced technologies potentially applicable in personalized treatments, EPMA J. 1 (2010) 164–209, https://doi.org/10.1007/s13167-010-0001-x.
[36] L.-L. Rui, H.-L. Cao, Y.-D. Xue, L.-C. Liu, L. Xu, Y. Gao, W.-A. Zhang, Functional organic nanoparticles for photodynamic therapy, Chin. Chem. Lett. 27 (2016) 1412–1420, https://doi.org/10.1016/j.cclet.2016.07.011.
[37] S. Kim, Y. Shi, J.Y. Kim, K. Park, J.X. Cheng, Overcoming the barriers in micellar drug delivery: loading efficiency, in vivo stability, and micelle-cell interaction, Expet Opin. Drug Deliv. 7 (2010) 49–62, https://doi.org/10.1517/17425240903380446.
[38] T.A. Debele, S. Peng, H.-C. Tsai, Drug carrier for photodynamic cancer therapy, Int. J. Mol. Sci. 16 (2015) 22094–22136, https://doi.org/10.3390/ijms160922094.
[39] L. Tang, J. Cheng, Nonporous silica nanoparticles for nanomedicine application, Nano Today 8 (2013) 290–312, https://doi.org/10.1016/j.nantod.2013.04.007.
[40] M.M. El-Hammadi, J.L. Arias, Recent advances in the surface functionalization of PLGA-based nanomedicines, Nanomaterials 12 (2022) 1–34, https://doi.org/10.3390/nano12030354.
[41] E.S. Lee, Y.S. Youn, Albumin-based potential drugs: focus on half-life extension and nanoparticle preparation, J Pharm Investig 46 (2016) 305–315, https://doi.org/10.1007/s40005-016-0250-3.
[42] S. Shah, H. Madhu, M. Soniwala, D. Mori, A. Vyas, A. Chauhan, B. Prajapati, Lipid-based nanoparticles, in: Nanocarrier Vaccines, Wiley, 2024, pp. 241–273, https://doi.org/10.1002/9781394175482.ch7.
[43] T.T.H. Thi, E.J.A. Suys, J.S. Lee, D.H. Nguyen, K.D. Park, N.P. Truong, Lipid-based nanoparticles in the clinic and clinical trials: from cancer nanomedicine to COVID-19 vaccines, Vaccines (Basel) 9 (2021), https://doi.org/10.3390/vaccines9040359.
[44] M. Vallet-regí, Chem. Soc. Rev. 51 (2022), https://doi.org/10.1039/d1cs00659b.
[45] K.B. Seljak, P. Kocbek, M. Gašperlin, Mesoporous silica nanoparticles as delivery carriers: an overview of drug loading techniques, J. Drug Deliv. Sci. Technol. 59 (2020), https://doi.org/10.1016/j.jddst.2020.101906.
[46] M. Vallet-Regí, M. Colilla, I. Izquierdo-Barba, M. Manzano, Mesoporous silica nanoparticles for drug delivery: current insights, Molecules 23 (2018), https://doi.org/10.3390/molecules23010047.
[47] F. Tang, L. Li, D. Chen, Mesoporous silica nanoparticles: synthesis, biocompatibility and drug delivery, Adv. Mater. 24 (2012) 1504–1534, https://doi.org/10.1002/adma.201104763.
[48] J. Lu, M. Liong, Z. Li, J.I. Zink, F. Tamanoi, Efficiency of Mesoporous Silica Nanoparticles for Cancer Therapy in Animals, 2010, pp. 1794–1805, https://doi.org/10.1002/smll.201000538.
[49] M. Vallet-Regi, A. Rámila, R.P. Del Real, J. Pérez-Pariente, A new property of MCM-41: drug delivery system, Chem. Mater. 13 (2001) 308–311, https://doi.org/10.1021/cm0011559.
[50] M. Colilla, M. Vallet-Regí, Organically modified mesoporous silica nanoparticles against bacterial resistance, Chem. Mater. 35 (2023) 8788–8805, https://doi.org/10.1021/acs.chemmater.3c02192.
[51] M. Vallet-Regí, F. Schüth, D. Lozano, M. Colilla, M. Manzano, Engineering mesoporous silica nanoparticles for drug delivery: where are we after two decades? Chem. Soc. Rev. 51 (2022) 5365–5451, https://doi.org/10.1039/D1CS00659B.
[52] E. Álvarez, M. Estévez, A. Gallo-Cordova, B. González, R.R. Castillo, M. del P. Morales, M. Colilla, I. Izquierdo-Barba, M. Vallet-Regí, Superparamagnetic iron oxide nanoparticles decorated mesoporous silica nanosystem for combined antibiofilm therapy, Pharmaceutics 14 (2022) 163, https://doi.org/10.3390/pharmaceutics14010163.
[53] A. García, B. González, C. Harvey, I. Izquierdo-Barba, M. Vallet-Regí, Effective reduction of biofilm through photothermal therapy by gold core@shell based mesoporous silica nanoparticles, Microporous Mesoporous Mater. 328 (2021) 111489, https://doi.org/10.1016/j.micromeso.2021.111489.
[54] Y. Wang, Q. Zhao, N. Han, L. Bai, J. Li, J. Liu, E. Che, L. Hu, Q. Zhang, T. Jiang, S. Wang, Mesoporous silica nanoparticles in drug delivery and biomedical applications, Nanomedicine 11 (2015) 313–327, https://doi.org/10.1016/j.nano.2014.09.014.
[55] A. Watermann, Mesoporous silica nanoparticles as drug delivery vehicles in cancer, Nanomaterials 7 (2017) 189, https://doi.org/10.3390/nano7070189.
[56] M. Vallet-Regí, M. Colilla, I. Izquierdo-Barba, M. Manzano, Mesoporous silica nanoparticles for drug delivery: current insights, Molecules 23 (2017) 47, https://doi.org/10.3390/molecules23010047.
[57] L. Beverina, M. Sassi, Twists and turns around a square: the many faces of squaraine Chemistry, Synlett 25 (2014) 477–490, https://doi.org/10.1055/s-0033-1340482.
[58] N. Barbero, C. Magistris, J. Park, D. Saccone, P. Quagliotto, R. Buscaino, C. Medana, C. Barolo, G. Viscardi, Microwave-assisted synthesis of near-infrared fluorescent indole-based squaraines, Org. Lett. 17 (2015) 3306–3309, https://doi.org/10.1021/acs.orglett.5b01453.
[59] C.Y. Lai, B.G. Trewyn, D.M. Jeftinija, K. Jeftinija, S. Xu, S. Jeftinija, V.S.Y. Lin, A mesoporous silica nanosphere-based carrier system with chemically removable CdS nanoparticle caps for stimuli-responsive controlled release of neurotransmitters and drug molecules, J. Am. Chem. Soc. 125 (2003) 4451–4459, https://doi.org/10.1021/ja028650l.
[60] S. Brunauer, P.H. Emmett, E. Teller, Adsorption of gases in multimolecular layers, J. Am. Chem. Soc. 60 (1938) 309–319, https://doi.org/10.1021/ja01269a023.
[61] E.P. Barrett, L.G. Joyner, P.P. Halenda, The determination of pore volume and area distributions in porous substances. I. Computations from nitrogen isotherms, J. Am. Chem. Soc. 73 (1951) 373–380, https://doi.org/10.1021/ja01145a126.
[62] A. Aguilar-Colomer, M. Colilla, I. Izquierdo-Barba, C. Jiménez-Jiménez, I. Mahillo, J. Esteban, M. Vallet-Regí, Impact of the antibiotic-cargo from MSNs on gram-positive and gram-negative bacterial biofilms, Microporous Mesoporous Mater. 311 (2021) 110681, https://doi.org/10.1016/j.micromeso.2020.110681.
[63] C.T. Kresge, M.E. Leonowicz, W.J. Roth, J.C. Vartuli, J.S. Beck, Ordered mesoporous molecular sieves synthesized by a liquid-crystal template mechanism, Nature 359 (1992) 710–712, https://doi.org/10.1038/359710a0.
[64] S. Fiorilli, B. Onida, B. Bonelli, E. Garrone, In situ infrared study of SBA-15 functionalized with carboxylic groups incorporated by a Co-condensation route, J. Phys. Chem. B 109 (2005) 16725–16729, https://doi.org/10.1021/jp045362y.
[65] C. Pontremoli, M. Boffito, R. Laurano, G. Iviglia, E. Torre, C. Cassinelli, M. Morra, G. Ciardelli, C. Vitale-Brovarone, S. Fiorilli, Mesoporous bioactive glasses incorporated into an injectable thermosensitive hydrogel for sustained Co-release of Sr2+ ions and N-acetylcysteine, Pharmaceutics 14 (2022) 1890, https://doi.org/10.3390/pharmaceutics14091890.
[66] M. Boffito, C. Pontremoli, S. Fiorilli, R. Laurano, G. Ciardelli, C. Vitale-Brovarone, Injectable thermosensitive formulation based on polyurethane hydrogel/mesoporous glasses for sustained co-delivery of functional ions and drugs, Pharmaceutics 11 (2019) 501, https://doi.org/10.3390/pharmaceutics11100501.
[67] T. Ohyashiki, M. Nunomura, T. Katoh, Detection of superoxide anion radical in phospholipid liposomal membrane by fluorescence quenching method using 1,3-diphenylisobenzofuran, Biochim. Biophys. Acta Biomembr. 1421 (1999) 131–139, https://doi.org/10.1016/S0005-2736(99)00119-4.
[68] Y. Prostota, O.D. Kachkovsky, L.V. Reis, P.F. Santos, New unsymmetrical squaraine dyes derived from imidazo[1,5-a]pyridine, Dyes Pigments 96 (2013) 554–562, https://doi.org/10.1016/j.dyepig.2012.10.006.

[69] E. Álvarez, M. Estévez, C. Jiménez-Jiménez, M. Colilla, I. Izquierdo-Barba, B. González, M. Vallet-Regí, A versatile multicomponent mesoporous silica nanosystem with dual antimicrobial and osteogenic effects, Acta Biomater. 136 (2021) 570–581, https://doi.org/10.1016/j.actbio.2021.09.027.

[70] M. Guembe, I. Izquierdo-Barba, B. González, M. Vallet-Regí, J. Díez, M. Colilla, D. Pedraza, Mesoporous silica nanoparticles decorated with polycationic dendrimers for infection treatment, Acta Biomater. 68 (2018) 261–271, https://doi.org/10.1016/j.actbio.2017.12.041.

[71] X. Hu, Y.Y. Huang, Y. Wang, X. Wang, M.R. Hamblin, Antimicrobial photodynamic therapy to control clinically relevant biofilm infections, Front. Microbiol. 9 (2018), https://doi.org/10.3389/fmicb.2018.01299.

[72] K. O'Riordan, O.E. Akilov, T. Hasan, The potential for photodynamic therapy in the treatment of localized infections, Photodiagnosis Photodyn. Ther. 2 (2005) 247–262, https://doi.org/10.1016/S1572-1000(05)00099-2.

[73] H.E. ElZorkany, T. Youssef, M.B. Mohamed, R.M. Amin, Photothermal versus photodynamic treatment for the inactivation of the bacteria Escherichia coli and Bacillus cereus: an in vitro study, Photodiagnosis Photodyn. Ther. 27 (2019) 317–326, https://doi.org/10.1016/j.pdpdt.2019.06.020.